Solid-state bonding of bulk PbTe to Ni electrode for thermoelectric modules

FERRERES, Xavier, GAZDER, Azdiar, MANETTAS, Abdrew and AMINORROAYA YAMINI, Sima <http://orcid.org/0000-0002-2312-8272>

Solid-state bonding of bulk PbTe to Ni electrode for thermoelectric modules

Xavier Reales Ferreres[1], Azdiar Gazder[2], Andrew Manettas[1], Sima Aminorroaya Yamini[1,3]*

Australian Institute for Innovative Materials (AIIM), Innovation Campus, University of Wollongong, Squires Way, North Wollongong , NSW 2500 , Australia

Electron Microscopy Centre (EMC), Innovation Campus, University of Wollongong, Squires Way, North Wollongong, NSW 2500, Australia

Department of Engineering and Mathematics, Sheffield Hallam University, City Campus, Sheffield S1 1WB, UK, S.Aminorroaya@shu.ac.uk

ABSTRACT:

The efficiency of thermoelectric generators is defined by the thermoelectric performance of materials, as expressed by the thermoelectric figure-of-merit, and their contacts with electrodes. Lead chalcogenide thermoelectric materials, and in particular PbTe, perform well in the 500 - 900 K temperature range. Here, we have successfully bonded bulk PbTe to Ni electrode to generate a diffusion barrier, avoiding continuous reaction of the thermoelectric legs and conducting electrodes at the operating temperature. We have modified the commonly used spark plasma sintering assembly method to join Ni electrode to bulk PbTe by driving the total supplied electrical current through the Ni and PbTe solid interfaces. This permits the formation of a thin diffusion layer, roughly 4.5 μm in thickness, which is solely

comprised of nickel telluride. This new technique towards the bonding of PbTe with the electrode is beneficial for thermoelectric materials, since high temperatures have proven to be damaging to the quality of bulk material. The interphase microstructure, chemical composition, and crystallographic information were evaluated by a scanning electron microscope equipped with electron back-scattered diffraction analysis. The obtained phase at the Ni/PbTe contact is found to be β_2 $Ni_{3\pm x}Te_2$ with a basic tetragonal crystallographic structure of the defective Cu_2Sb type.

KEYWORDS:

Solid-state bonding, spark plasma sintering, thermoelectric module, PbTe, Nickel electrode

1. INTRODUCTION

Recently, matters related to global warming have drawn attention worldwide [1,2] motivating sustainable energy projects [3] in order to address a possible future energy crisis [4]. Herein, thermoelectric devices have grown in importance [5], despite the fact that only low-temperature applications (up to 473 K) have been successfully commercialised [6]. Thermoelectric device efficiency and power output increase with temperature [7], indicating the need to reach higher temperatures, for instance 500 to 900 K, where lead chalcogenides and PbTe in particular are known to perform well [6,8]. This could take the technology into significant energy production, for example, in terrestrial applications, such as combustion engines in vehicles [9,10], industrial plants [11], or concentrating solar thermoelectric generators [12]. Despite the excellent thermoelectric figure-of-merit (zT) values for PbTe in both *n*- and *p*-type compounds [13-18], the performance of a device greatly depends on the quality of the junctions between the thermoelectric material and the metallic electrodes [19,20]. An example of such is the latest study on PbTe module which is bonded to Cu electrode through a $Co_{0.8}Fe_{0.2}$ interphase achieving at a maximum ΔT of 570 K an efficiency of approximately 9% [21].

In order to achieve good contact between materials, the junction must fulfil requirements such as mechanical stability, and homogeneity of the generated intermetallic. In our recent study, we have successfully bonded nickel electrode directly to *n*-type PbTe powder, where a homogenous diffusion barrier of 27 μm composed of nickel telluride was fabricated using the common spark plasma sintering (SPS) technique [22]. Nevertheless, tuning of the interphase thickness using the "one-step sintering" method [22] proved to be challenging, since the use of powder material in any electrical-current-based sintering process facilitates diffusion of elements [23], which, in this specific case, resulted in the formation of a thick interlayer at the contact. The control of interphase geometry is essential to the design of a thermoelectric generator (TEG) that is capable of achieving maximum power output and conversion efficiency at working temperatures [24,25]. In the current study, we investigate the possibility of generating an effective bond between bulk *p*-type PbTe to Ni plate when reducing the thickness of the generated diffusion barrier layer.

Spark plasma sintering apparatus was employed to join solid *p*-type PbTe bulk to Ni plate. The bonding of thermoelectric materials using SPS with different types of electrodes has been widely studied in recent years [22,26-28], although this sort of equipment was initially designed for the consolidation of powder. Both processes commonly entail the use of a graphite die, which is employed as housing for the powders. The intrinsic electrical current in any SPS process is distributed between the powder undergoing sintering and the graphite die throughout the entire time for the procedure. This distribution depends not only on the sample's electrical conductivity but on the different interface resistances appearing during the complex process of powder consolidation at the stages of heating, sintering, and cooling in the SPS. Other potential issues caused by the die-sample current distribution are seen as radial temperature gradients across the specimen, as well as localized Joule heating due to large current densities at the contact between the sample and the graphite die [23]. These could

cause even higher temperatures when joining two dissimilar materials with possible issues of sample melting. Moreover, the lower electrical resistance of graphite die at higher temperatures compared to that of PbTe, increases the complexity of current distribution across the assembly in the case of bonding two dissimilar materials. An effect of complex distribution of electrical current on the quality of sintered samples has been previously highlighted [29]. Therefore, in order to simplify our bonding assembly, we avoided the graphite die by using bulk PbTe instead of powder in order to force the total supplied current to pass through the PbTe and Ni, eliminating the possible interaction of the current with the die. Nevertheless, a large release of heat will still occur in the contact area between the Ni and the PbTe due to high current densities resulting from point contacts originating from the surface roughness of the materials [30].

This method resulted in the formation of a thin and homogenous interphase layer of β_2 phase nickel telluride ($Ni_{3\pm x}Te_2$). A detailed analysis of the crystallographic structures at the Ni/PbTe interface was conducted, which showed the appearance of ordered superstructures of the β_2 nickel telluride phase.

2. MATERIALS AND METHODS

Polycrystalline samples of $Pb_{0.985}Na_{0.015}Te$ were synthesized by mixing the stoichiometric ratio of high purity Pb (99.999%), Te (99.999%), and Na in vacuum-sealed quartz ampoules. Samples were heated to 1373 K and homogenised for 10 hours, followed by quenching in cold water. Afterwards, the samples were annealed at 823 K for 72 hours. The resulting ingots of *p*-type PbTe were hand-ground to powder with an agate mortar and a pestle. The obtained powder was consolidated into disks 12 mm in diameter and 1.5 mm thick using a Thermal Technology LLC, Model 10-4 Spark Plasma Sintering (SPS) apparatus at 793 K and 40 MPa axial pressure for 1 hour under vacuum.

The Seebeck coefficient and electrical resistivity of samples were measured using Linseis LSR-3 apparatus. The thermal conductivity ($\varkappa$) was calculated from $\kappa = \rho D_T C_p$. The laser flash method (Linseis LFA 1000) was used to measure the thermal diffusivity (D_T). The density (ϱ) was calculated using the measured weight and dimensions, and the specific heat capacity (C_p) was estimated by $C_p = 3.07 + 4.7 \times 10^{-4} \times (T[\mathrm{K}] - 300)$ [31,32].

The spark plasma sintering equipment is used to join the solid *p*-type PbTe bulk materials to Ni plates. This method can be described as solid-state interdiffusion bonding, where the thermocouple readings are used to adjust the system supplied electrical current in order to control the temperature for bonding. The SPS apparatus provided a pulsed DC current, which passed through both solid materials and the mating surfaces of PbTe and Ni. These surfaces were polished down to a roughness of 1 μm and ultrasonically cleaned with ethanol prior to the joining process in order to remove any possible contaminants. The pre-bonding thicknesses of the PbTe and Ni disks were approximately 1.5 mm and 0.3 mm, respectively. To proceed with the bonding, the assembly is sandwiched between layers of graphite foil inside the SPS chamber so to improve the thermal contact and distribution of force given by the graphite punches. The schematic illustration in Figure 1 shows the absence of a graphite die, therefore exposing the peripheral surfaces of PbTe and Ni to the chamber's atmosphere during the process of bonding. As a result, a possible radial variation in the interphase thickness could occur, which can be due to a temperature gradient in the sample's diameter caused by the increase in heat radiation loss when compared to the usage of a graphite die [23]. The temperature and holding time for the SPS procedure were optimised to achieve ideal bonding parameters, but nonetheless, the heating and cooling rates remained constant at 5 K/min for all samples.

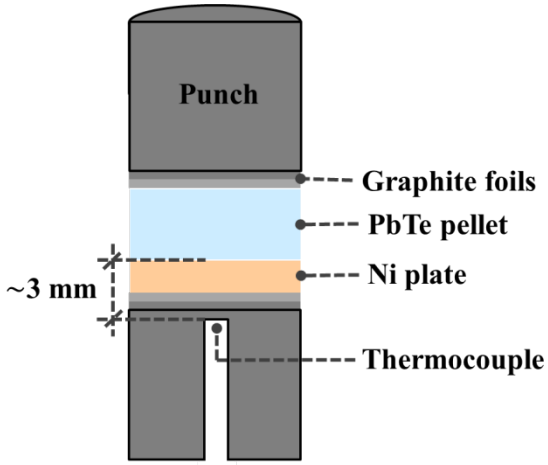

Figure 1. Experimental assembly for bonding between PbTe and Ni solids.

The thermal stability of PbTe sample after bonding to Ni plate was studied. The measurement of thermoelectric transport properties of the sample prior to bonding to Ni and after bonding was performed by mechanically removing the Ni plate and generated interphase using Struers Tegramin-20 automatic polisher. The electrical conductivity and Seebeck coefficient were measured using Linseis LSR-3 apparatus.

The electrical resistance of the interphase was measured using the Quantum Design PPMS equipment. Samples after performance of SPS bonding process were utilized for this purpose. The I-V curve was obtained to determine the ohmic contact resistance of Ni to *p*-type PbTe. Electrical currents below 100 mA were used to avoid Joule heating in the samples during measurement, while frequencies of 100 Hz were set to avoid Peltier effect. The final resistance value of interphase and contacts is obtained by subtracting the resistance values of PbTe and Ni from the total resistance of Ni+PbTe sample.

In order to study the microstructure of the interphase, joint samples were cut using Leica TXP Target Polisher equipment. Subsequently, cross-sections were mounted in conductive resin, polished, and analysed by scanning electron microscopy (SEM). Mechanical polishing

was used down to 1 μm, and the fine polished surfaces were prepared for electron back-scattered diffraction (EBSD) using ion milling on a Leica TIC-020.

EBSD results were obtained from a 69×13.5 μm^2 area using a JEOL JSM-7001F field emission-scanning electron microscope (SEM) operating at 15 kV, a roughly 6.5 nA probe current, and 1500× magnification. The microscope used a Nordys-II EBSD detector with Oxford Instruments Aztec software as interface. The conditions for EBSD mapping were previously calculated with 44, 42, and 40 reflectors employed for Ni, Ni_3Te_2 (virtual tetragonal), and PbTe phases, respectively, as well as 4×4 binning, 1 background frame, a Hough resolution of 60, and simultaneously indexed individual Kikuchi patterns up to 6 bands. The overall indexing rate for the raw EBSD map was 99%. The step size employed was 0.06 μm, which was equivalent to a map resolution of 1150×225 pixels.

4. RESULTS AND DISCUSSION

The interface temperature and the holding time for bonding are crucial parameters for the final quality of joint materials. We have optimised the joining temperature, holding time, and pressure to effectively bond *p*-type PbTe to Ni electrode. It is worth noting that similarity on coefficients of thermal expansion (CTE) between bonded materials is essential to avoid, at high temperature, strain to failure of bonded region. The CTE of PbTe ($20 \; x \; 10^{-6} \; K^{-1}$)[33] and Ni ($13.4 \; x \; 10^{-6} \; K^{-1}$) have shown to reasonably withhold at high temperatures [22,34].

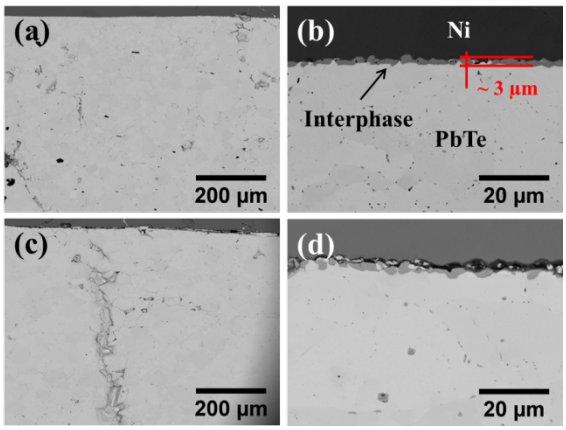

Figure 2. SEM micrographs of bonding areas at the PbTe/Ni interface after sintering under pressure of 20 MPa for 5 minutes (a, b), and 15 minutes (c, d) at temperature 623 K.

Figure 2(a) and (b) shows SEM micrographs of the fabricated interphase between PbTe and Ni plate, generated by sintering at 623 K, 20 MPa for 5 minutes. Figure 2(b) delineates a new phase at the PbTe/Ni interface, indicating the occurrence of a reaction between the initial counterparts. The thus-formed interphase presents no major signs of cracks or defects, similar to the PbTe side of the sample (Figure 2(a)). The average thickness of the interlayer is approximately 3 μm, and the discontinuity in the morphology is unwanted for application in a thermoelectric module. The lack of a defined barrier layer could lead to instability of the junction due to Ni diffusion into PbTe [35] or vice versa at the operating temperature of the device. Therefore, in order to increase the fabricated thickness and thus obtain a more homogeneous diffusion layer, the holding time for bonding was increased to 15 min (Figure 2(c) and (d)). The microstructure of the newly obtained interphase shows no improvement, indicating that time has, in this case, no significant effect on the thickness. In addition, the Ni and the intermediate layer are physically separated (Figure 2(d)), and there is also a significant amount of cracking on the PbTe side (Figure 2(c)). This suggests that during the Ni/PbTe reaction the holding time is a critical factor for the quality of bonding and the bonded disks.

The reaction occurring between Ni and PbTe is represented in chemical Equation (1), as is discussed in our recent study [22], which presents solid nickel telluride and liquid lead as the reaction products.

$$(3 \pm x)\mathrm{Ni(s)} + 2\mathrm{PbTe(s)} \rightarrow \mathrm{Ni}_{3\pm x}\mathrm{Te}_2\mathrm{(s)} + 2\mathrm{Pb(l)} \qquad \textbf{(1)}$$

Theoretical thermodynamic calculations based on chemical Equation (1) have identified 793 K as the temperature for spontaneous reaction (Gibbs free energy, $\Delta G < 0$) [22]. Experiments undertaken in the current study, however, indicate that 623 K is sufficient to initiate the solid-state reaction between Ni and PbTe (Figure 2). Given such realization, it is important to emphasise that the disparity between temperatures could be due to the extra amount of radiation loss coming from the sample's surface at the periphery in the newly proposed SPS assembly compared to our previous report [22],where the usage of a graphite die and its enveloping insulation prevented such losses from occurring. Additionally, the distance of roughly 3 mm between the end of the thermocouple and the Ni/PbTe reaction area, illustrated in Figure 1, is also a key factor for the experimental temperature reading due to the heat conduction through the bottom graphite punch. This separation was also presented in our recent study [22], suggesting that the sample's surface exposure in the current SPS assembly is also a cause for the low temperature read by the thermocouple.

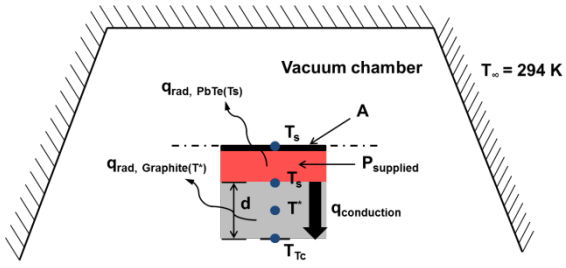

Figure 3. One-dimensional thermal model for the bonding process of current assembly in the SPS.

A one dimensional thermal model was performed (Figure 3) to determine the sample's temperature (T_s) (detailed in Supporting information). Figure 3 presents a schematic graph of the modelled assembly, which corresponds to half of the total SPS assembly due to its horizontal symmetry across the center of the Ni+PbTe sample. This model includes heat radiation from the sample and graphite punch as well as the heat conducted from the sample to the area where the thermocouple tip is located, which is at an exact distance of d = 3.2 mm. Equations 2, and 3 present the heat balance for the model. The supplied power by surface area (P/A), defined as $P_{supplied,}$ is half of the averaged value for peaks of power during the 5 minutes of sintering (see Figure S2 and S3 of Supporting information). The emissivity values for graphite ($\varepsilon_{Graphite}$) and lead telluride (ε_{PbTe}) are 0.95[36] and 0.98[37], respectively. Whereas, the conductivity coefficient for HPD grade graphite, provided by the supplier ($k_{Graphite}$) corresponds to 85 $Wm^{-1}K^{-1}$. It is assumed that the temperature of contact between sample and graphite punch is the same and equal to T_s, eliminating the heat conduction along the PbTe + Ni assembly. This approximate model highlights the significant difference of bonding temperatures between the current study and the theoretical temperature of formation for Ni_3Te_2 (793 K).

$$P_{supplied} = q_{conduction} + q_{rad,PbTe\,(T_s)} + q_{rad,Graphite\,(T^*)} \quad \textbf{(2)}$$

$$\frac{P}{A} = \frac{k_{Graphite}}{d}\,(T_s - T_{Tc}) + \varepsilon_{PbTe}\,\sigma\,(T_s^4 - T_\infty^4) + \varepsilon_{Graphite}\,\sigma\,\left(T^{*4} - T_\infty^4\right) \quad \textbf{(3)}$$

The average power for sample in Figure 2(b), at 623 K, corresponds to 426.55 W (Figure S2) which leads to a T_s of 764 K using Equation 3. This calculated temperature is lower than the theoretical temperature of formation for Ni_3Te_2, though this disparity is likely to be originated from the small quantity of nickel telluride generated at the contact (Figure 2(b)). The temperature values recorded by the thermocouple still allow us to investigate the

interphase evolution as a function of temperature and to maintain a constant experimental temperature during the holding process.

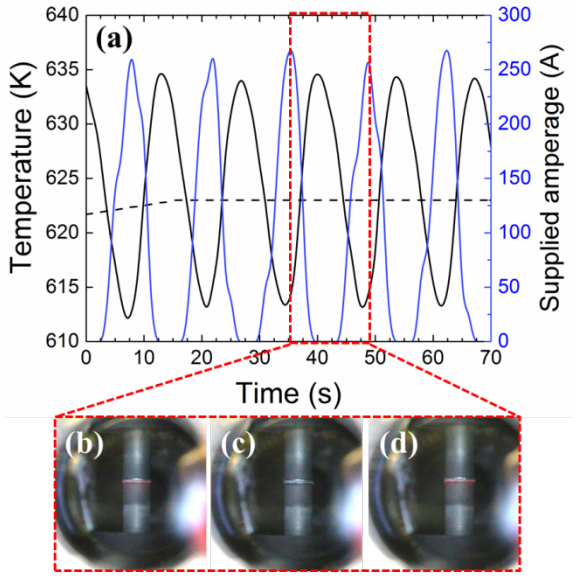

Figure 4. (a) SPS parameters of electric current (blue solid line), thermocouple temperature (black solid line), and temperature set point (black dashed line) during the holding time for the bonding procedure for the sample at 623 K, 20 MPa for 5 minutes; (b), (c), (d) frames extracted from a video of the bonding process, showing a red glow during spikes of supplied current.

Figure 4(a) presents the measured temperature, set point temperature, and supplied electric current at the beginning of the SPS holding time for the sample shown in Figure 2(a) and (b). The electric current is supplied via the equipment's proportional, integral, derivative (PID) process controller, using the measured temperature as the input variable to regulate the heating of assembly according to the pre-defined SPS program. The solid line for the measured temperature in Figure 4(a) shows constant fluctuations of ±20 K from the defined temperature set-point (dashed line), suggesting that the current PID settings struggle with the fast released heat at the Ni/PbTe interface, thus resulting in large oscillations of electrical current and temperature (both controlled by the PID). In order to better understand the

process, we have monitored the assembly during the bonding process (Figures 4(b) to (d)). The interface of PbTe/Ni glows red at the maximum peaks of current, with periodic cycles of 14 seconds, indicating that during oscillations of roughly 280 A (blue line) the interface temperature is ~ 900 K, when radiation becomes visible with wavelengths in the 700 nm region [38]. This suggests that the reaction shown in Equation (1) occurs during the peaks of current and that the short reaction times are not sufficient to generate a thick diffusion layer. Therefore, higher temperature, implying more current in the system via the PID controller, might be necessary to obtain a thicker diffusion barrier, since longer time has proven to be inefficient. Figures 2(c) and (d) shows that such oscillations in the current over an extended period of time have a significant effect on the quality of the interface, resulting in the separation of layers.

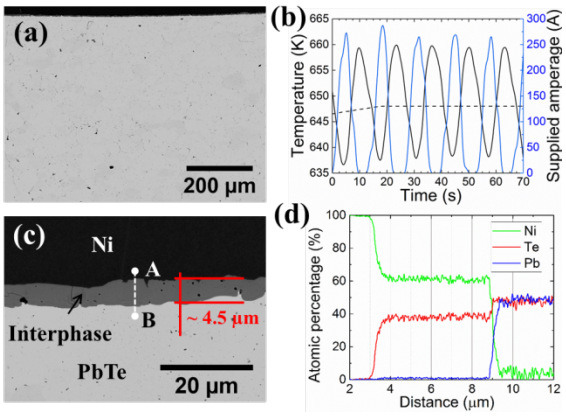

Figure 5. (a) SEM image of bonded sample generated during SPS bonding at 648 K, 20 MPa, and 5 minutes; (b) SPS parameters of supplied electrical current, thermocouple temperature, and temperature set-point illustrated by the blue solid line, the black solid line, and the black dashed line, respectively, for the same conditions expressed in (a); (c) higher magnification SEM micrograph of the sample in (a) to observe the thickness of the interphase; (d) line scan showing atomic percentages along AB line in (c).

Figure 5 shows the fabrication of interphase by increasing the bonding temperature, from 623 K (Figure 2) to 648 K, and consequently, the amplitude of oscillations in the electric current (Figure 5(b)). The sample temperature was approximated at 792.7 K through the model presented in Figure 3 and calculated using Equation 3 with a supplied power of $P_{supplied}$ = 438.75 W. A homogeneous reaction layer is formed at the interface between Ni and PbTe when they are bonded at 20 MPa for 5 minutes (Figure 5(c)). The generated interphase is roughly 4.5 μm thick and free of large porosity or cracks, indicating good cohesion between the layers. In addition, the distinct separation of the Ni electrode from the PbTe by the interlayer suggests the formation of an effective diffusion barrier. Figure 5(b) shows peaks of current close to 300 A, meaning that there was an increase on temperature due to more Joule heating than in the previous samples, these higher currents aid the Ni/PbTe reaction to form a thicker barrier layer. This and a visual analysis during the experimental process show that temperatures around 900 K were only generated at the contact and that the bulk of the PbTe was exposed to lower temperatures. This is viewed as an improvement of the new technique that promotes the bonding of PbTe with the electrode, since temperatures above 773 K have been proven to damage the quality of the bulk material.

Figure 5(d) show a line scan taken from point A to point B in Figure 5(c) which confirms no diffusion of elements in Ni and PbTe and a clear chemical separation of the Ni/interphase/PbTe phases. It also indicates that the interphase is solely composed of Ni and Te elements. The atomic percentage of Te element (roughly 38%) is indicative of the formation of a β_2 $Ni_{3\pm x}Te_2$ phase [39]. The formation of β_2 phase $Ni_{3\pm x}Te_2$ together with the absence of Pb at the contact are similar findings to those in our previous report on bonding of Ni plate to *n*-type PbTe powder using SPS [22]. Therefore, these results suggest strong thermal stability of the interphase when exposed to the operating temperature of the device. Furthermore, the electronic transport properties of PbTe before and after bonding with Ni

were measured to assess the thermal stability of PbTe during bonding procedure. Figure 6(a) and (b) show that the electronic transport properties of samples remain roughly the same after bonding process, indicating the joining method preserves the performance of thermoelectric material.

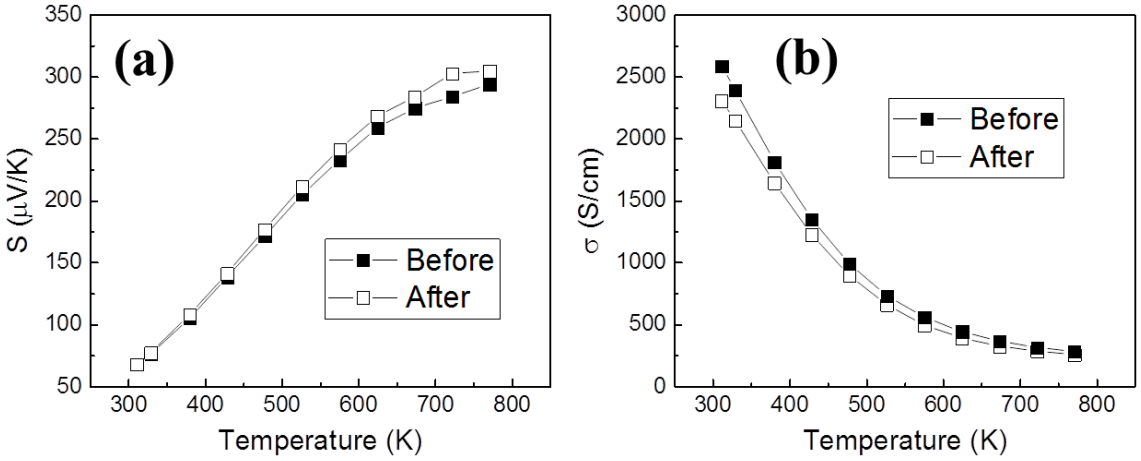

Figure 6. (a) Seebeck coefficients and (b) electrical conductivities of p-type PbTe samples before (solid symbols) and after (open symbols) SPS bonding with Ni electrode.

The electrical resistance for *p*-type PbTe bulk was measured at 1.36 mΩ, using measured room temperature resistivity of material and sample's dimensions, whereas the total resistance for the Ni+PbTe sample was 3.24 mΩ, calculated by the slope of Figure 7 (V-I curve), showing an ohmic behavior of bonded sample. The electrical resistance for Ni_3Te_2 and interface contacts with Ni and PbTe is of 1.87 mΩ, using a theoretical resistance of 3.2 x 10^{-3} mΩ for Ni plate.

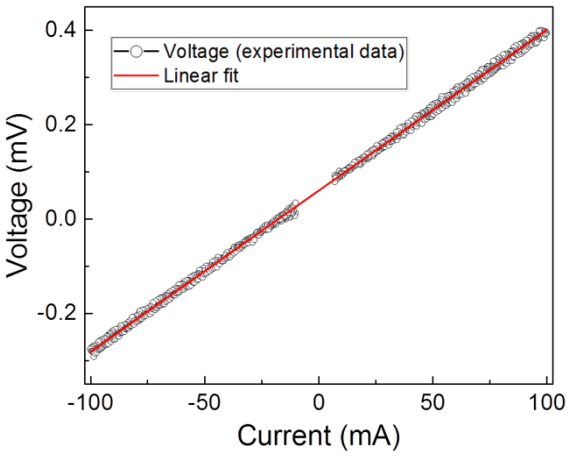

Figure 7. Experimental data (open symbols) for V-I curve of *p*-type PbTe bond to Ni plate and linear fit (solid line) indicating ohmic contact between the parts

The crystallographic structure of the interphase layer between Ni and PbTe was investigated using combined energy dispersive X-ray spectroscopy (EDS) and electron back-scattering diffraction (EBSD). The EDS results obtained from area maps and analysis of 20 random points within the interphase shows an average chemical composition of: Ni (at. % 61.92 ± 0.4687), and Te (at. % 38.08 ± 0.4687), indicating a chemical composition of $Ni_{3.3}Te_2$. This suggests that the interphase layer is solely composed of β_2 phase $Ni_{3\pm x}Te_2$ which nominally ranges in composition from $Ni_{0.61}Te_{0.39}$ to $Ni_{0.59}Te_{0.41}$ [39]. The $Ni_{3.3}Te_2$ phase has been described as having a monoclinic crystal symmetry, with corresponding lattice parameters a = 7.54 Å, b = 3.799 Å, c = 6.089 Å, and β = 91.2° [40], and with having the lowest enthalpy of formation for the three possible β_2 $Ni_{3\pm x}Te_2$ phases [41], hence being the stable compound at room temperature. Nevertheless, it is important to note that the monoclinic structure commonly ascribed to Ni_3Te_2 in previous studies is formed from a basic tetragonal of the defective Cu_2Sb-type [40]. Table 1 summarises the existing β_2 phases of $Ni_{3\pm x}Te_2$, as well as the transition temperatures within the phase: from monoclinic to orthorhombic [42] to tetragonal [43]. The nickel telluride system shows structural transition with temperature, caused by the

ordering of Ni atoms in the asymmetric unit cell [40], in addition to the close proximity of the lattice parameters of the phases.

Table 1. β_2 phase of $Ni_{3\pm x}Te_2$ with the corresponding crystallographic structures, lattice parameters, and their transition temperatures.

β_2 $Ni_{3\pm x}Te_2$	T of transition	Crystal structure	Lattice parameters				Ref
			a (Å)	*b* (Å)	*c* (Å)	*β* (°)	
Ni_3Te_2		Monoclinic	7.5382	3.7934	6.0883	91.159	[39,41]
$Ni_{2.88}Te_2$	491 K	Orthorhombic	7.5382	3.7879	6.0647	90	[39,41]
$Ni_{2.86}Te_2$	610 K	Tetragonal	3.7820	3.7820	6.0620	90	[39,40]

Figures 8(c) and (d) show the EBSD band contrast and phase distribution maps, respectively. Figure 8(d) illustrates top layer comprising large Ni grains (shown in red), whereas the middle and bottom layers contain multigrain Ni_3Te_2 (shown in blue), and PbTe (shown in green) phases, respectively. The non-indexed regions, shown in white in Figure 8(d), represent voids and porosities. It is worth noting that when the Ni_3Te_2 phase was first indexed as a monoclinic phase (Figure 8(a)), some grains presented with fictitious boundaries within grain interiors with angle-axis 90°/<001>, 180°/<100>, and 180°/<001>. These fictitious boundaries are representative of pseudo-symmetry in this phase which is caused by the mis-indexing of the monoclinic electron back-scattering patterns [44].

The detection of pseudo-symmetry in monoclinic Ni_3Te_2, is beneficial in that it predicts the possible phase transitions as well as the existence of a virtual parent structure [45]. These are in agreement with the particular case of the nickel telluride system, where the aforementioned ordering of Ni cations within the lattice gives rise to a structural relationship between high-temperature tetragonal and room-temperature monoclinic nickel telluride. In order to investigate the pseudo-symmetry, the PSEUDO program [45] (an online tool located on the

Bilbao Crystallographic server) was used to: (i) identify possible pseudo-symmetries in crystal structures and thereafter, (ii) calculate a virtual parent of a higher symmetry based on the minimum atomic displacement of the unit cell [45]. Consequently, the PSEUDO program checks if every atomic position in an initially defined crystal structure belonging to a lower symmetry space group can be described by a virtual crystal structure corresponding to a higher symmetry through small displacements to new atomic positions. In the present case of nickel telluride, the pseudo-symmetry in the monoclinic phase of space group 11 can be adequately described as a virtual tetragonal phase, space group 129 (shown in Figure 8(b)).

Figure 8(d) shows phase distribution map when Ni_3Te_2 is indexed as a virtual tetragonal (129) crystal structure. The interphase layer presents with no pseudo-symmetry whatsoever. It is to note that twins represented in red appear in the interphase and have 82.5° <110> angle-axis relationship with the parent matrix.

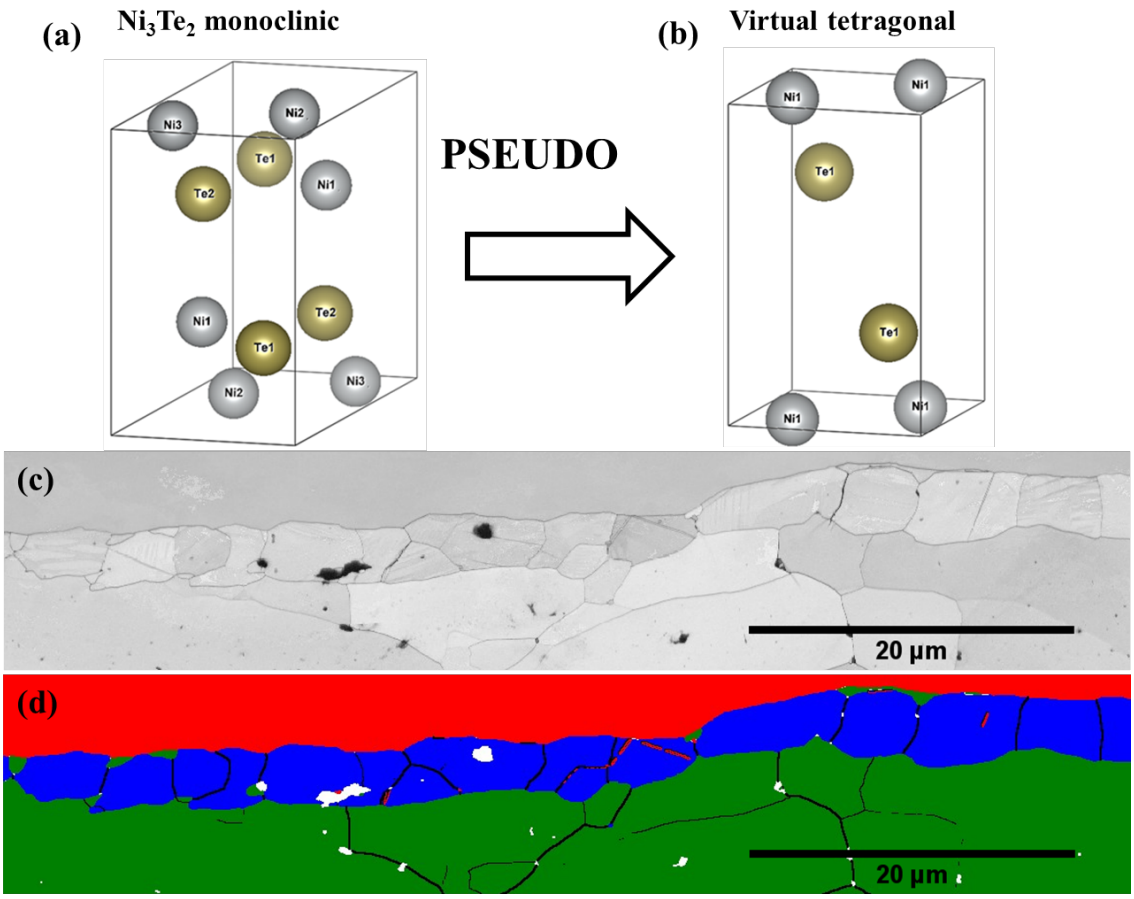

Figure 8. (a) Crystallographic structure for monoclinic Ni_3Te_2 (b) Tetragonal crystal structure assigned as the virtual parent of structure (a) obtained via PSEUDO program in order to detect and remove pseudosymmetry. (c) EBSD band contrast map, (d) EBSD phase distribution map with grain boundaries and twins using virtual tetragonal structure of (b).

4. CONCLUSIONS

The successful bonding of bulk *p*-type single-phase PbTe and Ni plate was achieved using a modified assembly method on a common type of SPS apparatus. Eliminating the graphite die during sintering forced the supplied electrical current to pass through the interface of the solids. The formation of a continuous and defect free interphase layer was obtained as thin as 4.5 μm when compared to then roughly 27 μm using powder PbTe together with a graphite die. This improvement is achieved due to consistent surface roughness of mating surfaces, obtained by mechanical polishing of bulk materials compared to powder sample. The

interphase layer is composed of solely monoclinic β_2 phase $Ni_{3\pm x}Te_2$. The observed pseudosymmetry at some grains during EBSD analysis suggested the existence of a virtual parent crystal with tetragonal symmetry, similar to the high temperature tetragonal $Ni_{2.86}Te_2$. This derived virtual tetragonal, with space group 129, shows higher indexation during EBSD, allowing for the study of the correct orientation of boundaries in the interphase layer.

ASSOCIATED CONTENT

Supporting Information

Additional details on the thermal model; equation for heat losses; power supplied by SPS during sintering of samples.

AUTHOR INFORMATION

Corresponding Author

*Email: S.Aminorroaya@shu.ac.uk (S.A.Y.)

Notes

The authors declare no competing financial interest.

ACKNOWLEDGMENTS

This work was supported by an Australian Research Council (ARC) Linkage Project (LP120200289), an ARC Discovery Early Career Research Award (DE130100310), and the AutoCRC 2020 (Project Agreement 1-203). The authors would like to thank the Electron Microscopy Centre (EMC) at the University of Wollongong for offering access to microscopes and sample preparation equipment.

REFERENCES

1 Peters, G. P.;Marland, G.;Le Quéré, C.;Boden, T.;Canadell, J. G.;Raupach, M. R. Rapid growth in CO2 emissions after the 2008-2009 global financial crisis. *Nature climate change* **2012**, 2, 2.

2 Cook, J.;Oreskes, N.;Doran, P. T.;Anderegg, W. R. L.;Verheggen, B.;Maibach, E. W.;Carlton, J. S.;Lewandowsky, S.;Skuce, A. G.;Green, S. A. Consensus on consensus: a synthesis of consensus estimates on human-caused global warming. *Environmental Research Letters* **2016**, 11, 048002.

3 Ellabban, O.;Abu-Rub, H.;Blaabjerg, F. Renewable energy resources: current status, future prospects and their enabling technology. *Renewable and Sustainable Energy Reviews* **2014**, 39, 748-764.

4 Qureshi, M. I.;Rasli, A. M.;Zaman, K. Energy crisis, greenhouse gas emissions and sectoral growth reforms: Repairing the fabricated mosaic. *Journal of Cleaner Production* **2016**, 112, 3657-3666.

5 Zheng, X. F.;Liu, C. X.;Yan, Y. Y.;Wang, Q. A review of thermoelectrics research–Recent developments and potentials for sustainable and renewable energy applications. *Renewable and Sustainable Energy Reviews* **2014**, 32, 486-503.

6 Snyder, G. J.;Toberer, E. S. Complex thermoelectric materials. *Nature Materials* **2008**, 7, 105-114.

7 Rowe, D. M. *CRC Handbook of Thermoelectrics: Macro to Nano*,CRC Taylor & Francis, 2006.

8 Fitriani;Ovik, R.;Long, B. D.;Barma, M. C.;Riaz, M.;Sabri, M. F. M.;Said, S. M.;Saidur, R. A review on nanostructures of high-temperature thermoelectric materials for waste heat recovery. *Renewable and Sustainable Energy Reviews* **2016**, 64, 635-659.

9 Qiang, J. W.;Yu, C. G.;Deng, Y. D.;Su, C. Q.;Wang, Y. P.;Yuan, X. H. Multi-objective optimization design for cooling unit of automotive exhaust-based thermoelectric generators. *Journal of Electronic Materials* **2016**, 45, 1679-1688.

10 Ibrahim, E. A.;Szybist, J. P.;Parks, J. E. Enhancement of automotive exhaust heat recovery by thermoelectric devices. *Proceedings of the Institution of Mechanical Engineers, Part D: Journal of Automobile Engineering* **2010**, 224, 1097-1111.

11 Ebling, D. G.;Krumm, A.;Pfeiffelmann , B.;Gottschald, J.;Bruchmann, J.;Benim, A. C.;Adam, M.;Labs, R.;Herbertz, R. R.;Stunz, A. Development of a system for thermoelectric heat recovery from stationary industrial processes. *Journal of Electronic Materials* **2016**, 45, 3433-3439.

12 Kraemer, D.;Jie, Q.;McEnaney, K.;Cao, F.;Liu, W.;Weinstein, L. A.;Loomis, J.;Ren, Z.;Chen, G. Concentrating solar thermoelectric generators with a peak efficiency of 7.4%. *Nature Energy* **2016**, 1, 16153.

13 Heremans, J. P.;Jovovic, V.;Toberer, E. S.;Saramat, A.;Kurosaki, K.;Charoenphakdee, A.;Yamanaka, S.;Snyder, G. J. Enhancement of thermoelectric efficiency in PbTe by distortion of the electronic density of states. *Science* **2008**, 321, 554-557.

14 Androulakis, I.;Todorov, I.;Chung, D. Y.;Ballikaya, S.;Wang, G.;Uher, C.;Kanatzidis, M. High thermoelectric efficiency in co-doped degenerate *p*-type PbTe. *MRS Proceedings* **2010**, 1267.

15 Vineis, C. J.;Shakouri, A.;Majumdar, A.;Kanatzidis, M. G. Nanostructured thermoelectrics: big efficiency gains from small features. *Advanced Materials* **2010**, 22, 3970-3980.

16 Biswas, K.;He, J.;Blum, I. D.;Wu, C. I.;Hogan, T. P.;Seidman, D. N.;Dravid, V. P.;Kanatzidis, M. G. High-performance bulk thermoelectrics with all-scale hierarchical architectures. *Nature* **2012**, 489, 414.

17 LaLonde, A. D.;Pei, Y.;Snyder, G. J. Reevaluation of $PbTe_{1-x}I_x$ as high performance n-type thermoelectric material. *Energy & Environmental Science* **2011**, 4, 2090-2096.

18 Zhao, L. D.;Dravid, V. P.;Kanatzidis, M. G. The panoscopic approach to high performance thermoelectrics. *Energy & Environmental Science* **2014**, 7, 251-268.

19 Kim, Y.;Yoon, G.;Park, H. S. Direct Contact Resistance Evaluation of Thermoelectric Legs. *Experimental Mechanics* **2016**, 56, 861-869.

20 Xia, H.;Drymiotis, F.;Chen, C. L.;Wu, A.;Chen, Y. Y.;Snyder, G. J. Bonding and high-temperature reliability of NiFeMo alloy/n-type PbTe joints for thermoelectric module applications. *Journal of Materials Science* **2015**, 50, 2700-2708.

21 Hu, X.;Jood, P.;Ohta, M.;Kunii, M.;Nagase, K.;Nishiate, H.;Kanatzidis, M. G.;Yamamoto, A. Power generation from nanostructured PbTe-based thermoelectrics: comprehensive development from materials to modules. *Energy & Environmental Science* **2016**, 9, 517-529.

22 Reales Ferreres, X.;Aminorroaya Yamini, S.;Nancarrow, M.;Zhang, C. One-step bonding of Ni electrode to n-type PbTe–a step towards fabrication of thermoelectric generators. *Materials & Design* **2016**, 107, 90-97.

23 Guillon, O.;Gonzalez-Julian, J.;Dargatz, B.;Kessel, T.;Schierning, G.;Räthel, J.;Herrmann, M. Field-assisted sintering technology/spark plasma sintering: mechanisms,

materials, and technology developments. *Advanced Engineering Materials* **2014**, 16, 830-849.

24 Rowe, D. M.;Min, G. Evaluation of thermoelectric modules for power generation. *Journal of Power Sources* **1998**, 73, 193-198.

25 Bjørk, R. The universal influence of contact resistance on the efficiency of a thermoelectric generator. *Journal of Electronic Materials* **2015**, 44, 2869-2876.

26 Fan, J.;Chen, L.;Bai, S.;Shi, X. Joining of Mo to $CoSb_3$ by spark plasma sintering by inserting a Ti interlayer. *Materials Letters* **2004**, 58, 3876-3878.

27 de Boor, J.;Gloanec, C.;Kolb, H.;Sottong, R.;Ziolkowski, P.;Müller, E. Fabrication and characterization of nickel contacts for magnesium silicide based thermoelectric generators. *Journal of Alloys and Compounds* **2015**, 632, 348-353.

28 Kraemer, D.;Sui, J.;McEnaney, K.;Zhao, H.;Jie, Q.;Ren, Z. F.;Chen, G. High thermoelectric conversion efficiency of MgAgSb-based material with hot-pressed contacts. *Energy & Environmental Science* **2015**, 8, 1299-1308.

29 Locci, A. M.;Cincotti, A.;Todde, S.;Orrù, R.;Cao, G. A methodology to investigate the intrinsic effect of the pulsed electric current during the spark plasma sintering of electrically conductive powders. *Science and technology of advanced materials* **2010**, 11.

30 Kazakov, N. F. *Diffusion bonding of materials*.,Mashinostroenie, 1981.

31 Blachnik, R.;Igel, R. Thermodynamische Eigenschaften von IV–VI-Verbindungen: Bleichalkogenide/thermodynamic properties of IV–VI-compounds: Leadchalcogenides. *Zeitschrift für Naturforschung B* **1974**, 29, 625-629.

32 Pashinkin, A. S.;Mikhailova, M. S.;Malkova, A. S.;Fedorov, V. A. Heat capacity and thermodynamic properties of lead selenide and lead telluride. *Inorganic Materials* **2009**, 45.

33 Hikage, Y.;Masutani, S.;Sato, T.;Yoneda, S.;Ohno, Y.;Isoda, Y.;Imai, Y.;Shinohara, Y. *26th International Conference on Thermoelectrics*. 331-335.

34 Xia, H.;Drymiotis, F.;Chen, C. L.;Wu, A.;Snyder, G. J. Bonding and interfacial reaction between Ni foil and n-type PbTe thermoelectric materials for thermoelectric module applications. *Journal of Materials Science* **2014**, 49, 1716-1723.

35 George, T. D.;Wagner, J. B. Diffusion of nickel and chlorine into lead telluride II. diffusion at the phase limits. *Journal of The Electrochemical Society* **1969**, 116, 848-854.

36 Fuschillo, N.;Gibson, R. Germanium-silicon, lead telluride, and bismuth telluride alloy solar thermoelectric generators for venus and mercury probes. *Advanced Energy Conversion* **1967**, 7, 43-52.

37 Neuer, G. Spectral and total emissivity measurements of highly emitting materials. *International Journal of Thermophysics* **1995**, 16, 257-265.

38 Tipler, P. A.;Meyer-Arendt, J. R. College physics. *Applied Optics* **1987**, 26, 5220.

39 Ball, R. G. J.;Dickinson, S.;Cordfunke, E. H. P.;Konings, R. J. M.;Drowart, J.;Smoes, S. (Commission of the European Communities, 1992).

40 Kok, R. B.;Wiegers, G. A.;Jellinek, F. The system nickel-tellurium I. Structure and some superstructures of the $Ni_{3\pm q}Te_2$ phase (preliminary communication). *Recueil des Travaux Chimiques des Pays-Bas* **1965**, 84, 1585-1588.

41 Gulay, L. D.;Olekseyuk, I. D. Crystal structures of the compounds Ni_3Te_2, $Ni_{3-\delta}Te_2$ (δ= 0.12) and $Ni_{1.29}Te$. *Journal of alloys and compounds* **2004**, 376, 131-138.

42 Grønvold, F. Heat capacities and thermodynamic properties of hexagonal and liquid selenium in the range 298 to 1000 K. Enthalpy and temperature of fusion. *The Journal of Chemical Thermodynamics* **1973**, 5, 525-531.

43 Mills, K. C. Heat capacity of nickel and cobalt tellurides. *Journal of the Chemical Society, Faraday Transactions 1: Physical Chemistry in Condensed Phases* **1974**, 70, 2224-2231.

44 Karthikeyan, T.;Dash, M. K.;Saroja, S.;Vijayalakshmi, M. Evaluation of misindexing of EBSD patterns in a ferritic steel. *Journal of microscopy* **2013**, 249, 26-35.

45 Capillas, C.;Tasci, E. S.;de la Flor, G.;Orobengoa, D.;Perez-Mato, J. M.;Aroyo, M. I. A new computer tool at the bilbao crystallographic server to detect and characterize pseudosymmetry. *Zeitschrift für Kristallographie Crystalline Materials* **2011**, 226, 186-196.